Pressure Measurements using an Airborne Differential Absorption Lidar. Part I: Analysis of the systematic error sources

Cyrille N. Flamant[1]

University of Maryland, College Park, Maryland

Geary K. Schwemmer[2], C. Laurence Korb

Laboratory for Atmospheres

NASA Goddard Space Flight Center, Greenbelt, Maryland

Keith D. Evans

Joint Center for Earth Systems Technology

University of Maryland Baltimore County, Baltimore, Maryland

Stephen P. Palm

Science Systems and Applications Inc., Seabrook, Maryland

[1]Current affiliation: Service d'Aéronomie du CNRS, Université Pierre et Marie Curie, Paris, France

[2]Corresponding author address: NASA Goddard Space flight Center, Code 912, Greenbelt, Maryland 20771.

Abstract

Remote airborne measurements of the vertical and horizontal structure of the atmospheric pressure field in the lower troposphere are made with an oxygen differential absorption lidar (DIAL). A detailed analysis of this measurement technique is provided which includes corrections for imprecise knowledge of the detector background level, the oxygen absorption line parameters, and variations in the laser output energy. In addition, we analyze other possible sources of systematic errors including spectral effects related to aerosol and molecular scattering, interference by rotational Raman scattering and interference by isotopic oxygen lines.

Key words: DIfferential Absorption Lidar, Pressure, Raman, Oxygen Isotopic Line

1. Introduction

Measurement of atmospheric pressure field is desirable for improving weather forecasting in the mid-latitudes, since the location of high and low pressure areas determine the weather patterns. Furthermore, the storm regime and fronts are an important weather phenomena and produce significant air-sea interaction and planetary boundary layer (PBL) fluxes (Brown and Levy, 1986). The frontal location and mesoscale dynamics of midlatitude storm systems are difficult to define with conventional analysis, partly because of mesoscale variability in both the atmosphere and ocean, which is generally

observed to be very large. Bond and Feagle (1985) suggested that atmospheric dynamics take place on scales that are not practically resolvable with conventional methods.

Better determination of the winds, stress, sea surface temperature and frontal location are essential for progress in these mesoscale modeling efforts. Nuss and Brown (1987) have shown that the primary limitation on the accuracy of the models was the sparsity of the input data. Remote sensing instruments are likely candidates to supplement the existing observational network with additional data at a density usable for routine synoptic-scale analyses.

Experiments incorporating scatterometer wind data in the European Center for Medium Range Weather Forcasts forecasting model have shown great potential for improved forcasting skills in the Southern Hemisphere (Anderson *et al.*, 1987). In order to relate this data to conventional analysis a good representation of the stress, roughness, stratification, PBL winds and upper level flow with corresponding pressure fields must be established. Levy and Brown (1991) tested the existing method of integrating the *Seasat-A* Satellite Scatterometer (SASS) wind data to provide surface-pressure analyses in the Southern Hemisphere and compared the results with standard operational analysis products. SASS-derived winds were input in a PBL model to construct surface-pressure fields (Brown and Levy, 1986). Their fields were found in good agreement (within 1-2 hPa) with the National Meteorological Center analyses in the Northern Hemisphere. In addition, the comparisons also revealed some sub-synoptic-scale variability that was not shown in the National Meteorological Center analyses.

Differential absorption lidar (DIAL) provides the only direct remote measurement of atmospheric pressure with high spatial resolution and precision. The theory of using the DIAL technique to measure atmospheric pressure has been described by Korb and Weng (1983). The lidar system used in these measurements has been described by Schwemmer *et al.* (1987), and earlier measurements from ground and aircraft reported have been by Korb *et al.* (1989) and Starr *et al.* (1992). We describe here the detailed analysis of the various potential systematic error sources to DIAL pressure measurements. In a companion paper (hereon referred to as Part II) we describe the development and application of the correction techniques as applied to a series of measurements made from an aircraft off the east coast of the United States during June and July of 1989.

High spectral resolution DIAL is a particularly complicated technique, both from an instrumental perspective and from an analysis perspective. The pressure measurement is usually more forgiving than DIAL measurements of temperature and specific humidity that operate with a laser centered on narrow absorption lines. This is because the pressure measurement is made in the much broader, flatter absorption trough between lines. There are still, however, many opportunities for systematic errors to enter the data. Thus, we have attempted to evaluate as many sources of error as possible within this study before applying corrections to the data collected from the flight experiments.

The instrument typically must include one or more tunable high spectral resolution lasers, preferably single frequency with very high spectral purity, i.e. very low broadband emission or out of band frequencies. One laser, the

on-line laser, is tuned to the oxygen spectral absorption feature of interest, while the second, off-line laser is tuned to a nearby unabsorbed frequency. The lasers are fired nearly simultaneously and the resulting two return signals must be accurately superimposed in order to be able to ratio them to determine the atmospheric transmission as a function of range or altitude. Since the data is digitally sampled at discrete time intervals, the time (or range) of any given sample in one laser return must accurately correspond to the time (or range) of the corresponding sample in the other laser return signal. Backscatter by molecules is double doppler broadened, and has a width equal to twice the doppler width of the absorption lines. On the other hand, the backscatter from aerosols is very narrow and is spectrally identical to the outgoing laser emission (ignoring any doppler shift caused by the bulk motion of aerosols, which is negligible compared to the width of the oxygen absorption lines). Effects due to this complexity have been discussed by Korb and Weng (1982) for temperature measurements, and by Ansmann (1985) as well as Ansmann and Bosenberg (1987) with respect to water vapor measurements. Accordingly, a measurement of the aerosol to molecular backscatter ratio must be derived from the off-line (or reference) return signal. In addition, oxygen and nitrogen rotational Raman scattering contribute a signal, which is over 3% of the molecular backscatter, if not filtered out, as is the case with the measurements discussed in Part II. Since rotational Raman backscatter is spectrally spread out over tens of wavenumbers from the laser frequency, it is only weakly absorbed on the return path to the lidar receiver, and can dominate the on-line return signal from large distances. These and other systematic effects are carefully evaluated in the following analysis.

In Section 2 we describe the data acquisition equipment. Section 3 describes instrumental effects and Section 4 atmospheric effects. The error sources are discussed from the perspective of having observed anomalously high pressure retrievals in regions of high aerosol backscatter.

2. Description of the data acquisition

Nighttime measurements were made with a dual alexandrite laser lidar system mounted in a nadir pointing position in the NASA Electra aircraft. The laser beams had a divergence of about 2.5 mrad. Pressure was derived from measurements of the atmospheric transmission in the trough region between the RR13 and RQ14 lines of the oxygen A-band, at a vacuum wavenumber of 13,152.38 cm^{-1}, or 760.32 nm wavelength in surface pressure air. The off-line or reference laser wavelength was 757.49 nm. The receiver contained a red pass filter, blocking wavelengths below 720 nm. The detector, a multialkali photomultiplier tube (PMT) had a gain of approximately 2×10^4 and was followed by a transimpedence amplifier with a gain of 3,000 volts/amp. The PMT was gated on a few microseconds after the laser pulse, and kept on for about 100 μs. The amplifier output signal was fed through a 2 MHz single pole low pass filter to a transient recorder with a 12 bit A/D converter sampling at a 5 MHz rate, which corresponds to 30 m altitude intervals. Five hundred samples were stored in the transient recorder memory, corresponding to the time the PMT was gated on to the time it was gated off. The digitizer clock was rephased with each laser pulse to a measured accuracy of better than 1 ns. The on-line laser was fired first, then 300 μs latter the

off-line laser was fired, the digitizer clock was again rephased, and another 500 samples containing the off-line return signal were stored. A few milliseconds before the next pulse pair, the data acquisition system was triggered to make a background measurement which was subtracted from the set of laser return signals that followed. The entire sequence was repeated every 100 ms, and all data were recorded.

Since the aircraft was flown at an altitude between 3600 m and 4200 m, the return signals include the strong surface reflection and about 75 μs of data after that, which contains information on the behavior of the PMT in response to strong signals. We used a notch in the gating pulse to reduce the amplitude of the electrical impulse associated with the surface return. A second photomultiplier was used as an altimeter. It was connected to a time to digital converter which counted 80 MHz clock pulses from the rephased master clock from which the digitizer clock was derived. By counting the number of clock pulses from the time the laser fired to the time the surface reflection arrived at this PMT, we measured the aircraft altitude to a resolution of 1.9 m. The altimeter was calibrated to an absolute accuracy at this resolution by ranging to a hard target while the aircraft was situated on the ground and comparing the result to a second, calibrated laser ranger. Having the altimeter measurement made simultaneously with the pressure measurement is important for establishing an absolute calibration to the pressure measurements. we note that the pressure drops about 1 hPa for every 10 m increase in altitude near the surface.

In addition to the lidar system, a Navigation and Environmental Measurements System (NEMS) collected data from a Loran navigation instrument,

aircraft pitch and roll from gyroscopes, cabin pressure, outside air temperature, dew point, and static pressure. Radiosonde balloons were launched from Wallops Island at the beginning of each flight and hourly thereafter. The balloons were tracked by radar to determine their geometric altitude and the wind vector as they ascended.

3. Instrumental error sources

a. Ambient light background and lidar signal baseline subtraction

Five milliseconds prior to firing the laser, the data system acquires the background of ambient atmospheric light scattered in the direction of the telescope. The background signal is then subtracted from the subsequent lidar return signals in real time and the signal minus background was recorded on tape. The gain of the PMT changes during the transient however, so we routinely exclude at least the first microsecond of data from analysis. An error in the measurement and subtraction of the background signal will have the same effect as an error in the lidar signal baseline discussed next.

PMTs typically exhibit an elevated dark current for some time after exposure to a bright light source, even to some extent if the PMT was off when exposed. Lidar return signal data is recorded between the altitude of the aircraft to the equivalent of 11 km below the surface. In previous work by Korb *et al.* (1989) and Starr *et al.* (1992), the return signal below the surface was used to define a baseline reference for each shot to correct for this signal induced bias. Strong backscatter signal is usually received from the near-field backscatter, from clouds and the surface return. Near-field blinding of the

PMT is eliminated by setting to zero the voltage between the photocathode and the first dynode for a few microseconds. Then the digitization gates were open 100 μs, long enough for the saturated signal to decay to a suitable baseline value. Previously, Korb *et al.* (1989) would average 100 values along the tail end of the signal, then subtract from the near field return a value equal to this tail value and assume it is constant throughout the signal, which is not strictly true. An improved PMT (Hamamatsu R1017) was used for the data discussed here and was tested in the laboratory prior to its use in the field. Lee *et al.* (1989) have measured the response function of this PMT, which after the first 10 μs, decays exponentially with a 7 μs time constant. They found that an unsaturated pulse peak should have a negligible baseline value (close to zero). Therefore, we applied no such extra baseline subtraction to the data discussed here. Verification of the background subtraction and baseline assumption was made by introducing a baseline shift to our measured signals, reprocessing the data to retrieve 125 pressure profiles along one flight track. The mean of the differences between the radiosonde and the lidar pressures, and the variance at each altitude in the lidar data are a minimum without any baseline shift. Shifts of ± 10 counts ($\approx$2% of the median signal level) induces an average 3 hPa bias, unevenly distributed with altitude and peaking at about 6 hPa at an altitude of 1500 m. It also increases the standard deviation along the flight track from 4.0 hPa to 4.3 hPa. The standard deviations were taken at each altitude using the 125 pressure profiles along the flight track, not from the 100 signal average used to make each pressure retrieval, so they include atmospheric variance. The latter had standard deviations of 1 to 2 hPa.

b. Laser blocked data and off-line/off-line lidar data

To test for possible ground loops in the signals, we looked at in-flight acquired data in which the laser beams were blocked from exiting the aircraft. We also took data with both lasers tuned to the same off-line frequency, which we call off-off data, to check the signal altitude registration and the background subtraction.

For blocked data measurements, the regular background and return signal recording sequence takes place without the laser beam going out to the atmosphere so that the signal detected for both acquisitions should be proportional to the atmospheric background. In the case where no ground loop exists and without the background subtraction, the ratio of the on-line to the off-line should be equal to unity and not vary with range but should be noisy because of the small quantities being ratioed. In the case of a ground loop, the strong flash lamp current pulse ($\geq$ 100 A) will perturb the potential of the local ground which manifests itself as a signal in single ended inputs if there is a ground current path for this pulse through the detection system. The receiver will register an output signal added to the background, and the ratio of the on-line to off-line signal will not be unity or constant with range. Ground loops are eliminated by careful design of the electronics and data acquisition system, and through testing, ensuring there is only a single ground path from the detector to earth ground, and that no part of it includes laser electronics. This was tested with an Ohmmeter and a floating oscilloscope set to a gain of 100μ volts/div. Other than the small transient due to the switching of the gate voltage, there was no evidence of a ground loop on the

receiver signals at the 10 μV limiting resolution, which corresponds to 0.04 counts. Nor was ground loop interference found to affect the recorded data (Figure 1).

Off-off measurements are made in-flight by tuning both lasers to the same wavelength, corresponding in this case to the off-line wavelength. If the lasers sample the same atmospheric layer at the same time, the return signal on both channels should be proportional and their ratio should be constant with altitude. If one channel starts recording before the other, aerosol features will not be registered at the same altitude and large oscillations in the ratio of the two signals will be generated. Except for some near-field discrepancies which are due to slightly different divergence characteristics of the two lasers, the signal ratio yields a constant with altitude. Note that a relatively large (8 mrad) telescope field of view (FOV) creates an overlap function that quickly converges to unity, at about 50 meters distance.

c. Aircraft pitch, roll and altitude corrections

The nadir direction for the outgoing laser beam is calculated so as to account for the nominal in-flight aircraft pitch angle of +2° (nose up). On the ground, the airplane pitch angle is -2°, so the laser beam is aligned toward the back of the aircraft at a 4° angle from the vertical when on the ground. In flight, the beam is pointing straight down.

Both pitch and roll are measured using gyros, and the data is recorded on the NEMS acquisition computer. In the post-experiment analysis, we generate 100-shot averaged lidar profiles, and add the NEMS data to the records and use the roll and pitch information to correct the altitudes of the backscat-

tered signals and the optical depths.

The altitude of the aircraft is measured from the signal reflected off the surface and is corrected for the pitch and roll angles and an 18 m calibration offset. Neglecting the aircraft displacement during the lase pulse round-trip time (3 mm at a 4 km altitude for a speed of 120 $\mathrm{m\,s^{-1}}$), we assume that the laser beam round-trip is achieved on the same path. If the surface reflection signal is not above the altimeter discriminator threshold, an erroneous altitude retrieval results. Those shots were filtered out (on the order of 10 per flight leg).

d. Laser energy normalization and calibration of atmospheric transmission versus pressure

The return signal intensity for both the on-line and off-line signals are range-squared corrected as well as laser energy corrected. The latter correction is done using energy monitor values, made with a photoconductive silicon photodiode and a charged integrating digitizer that integrates over the 100 ns laser pulse. Corrections are made according to:

$$S_i(z) = \frac{1}{N}\sum_{j=1}^{N}\left(\frac{S_{ij}(z)}{E_{ij}}\right) \times \overline{E_i} \qquad \text{where} \qquad \overline{E_i} = \frac{1}{N}\sum_{j=1}^{N} E_{ij}, \tag{1}$$

where i can be read as on-line or off-line, j is the shot number, N is number of shots, E is the energy monitor value and S is the lidar signal value.

The optical power received goes through the detection chain and the output signal, $S(z)$, is given as a number of counts per unit time, related to the optical power, $P(z)$, by:

$$S(z) = \frac{P(z)}{h\,\nu\,c}\,G\,e^{-}\,R_e\,D \tag{2}$$

where h is Plank's constant, ν is the laser off-line or on-line wavenumber, G is the gain of the PMT dynode chain, e^- is the charge of an electron, D is the volts to counts (analog to digital) conversion factor, c is the speed of light and R_e is the equivalent resistance of the transimpedence amplifier.

Since both on-line and off-line signals are made with a single detector and both energy monitor signals are made with a single detector, then in calculating the transmission, all constants will factor out and the transmission profile, $\tau(z)$, is given as:

$$\tau(z) = \left(\frac{P_{on}(z)}{P_{off}(z)}\right) \times \left(\frac{E_{off}}{E_{on}}\right), \tag{3}$$

where P_{on} and P_{off} are the detected optical power for the on-line and off-line channel (ignoring any molecular broadening), respectively given by:

$$\begin{aligned} P_{on}(z) &= \frac{A\,T_0}{(z_{ref}-z)^2}\,\eta\,E_{on}\,\frac{c}{2}\,(\beta_{p,on}(z)+\beta_{m,on}(z)) \\ &\quad \exp\left(-2\int_{z_{ref}}^{z}(K(r)+\alpha_{p,on}(r)+\alpha_{m,on}(r))\,dr\right) \end{aligned} \tag{4a}$$

and

$$\begin{aligned} P_{off}(z) &= \frac{A\,T_0}{(z_{ref}-z)^2}\,\eta\,E_{off}\,\frac{c}{2}\,(\beta_{p,off}(z)+\beta_{m,off}(z)) \\ &\quad \exp\left(-2\int_{z_{ref}}^{z}(\alpha_{p,off}(r)+\alpha_{m,off}(r))\,dr\right) \end{aligned} \tag{4b}$$

where η is the detector quantum efficiency at 760 nm[3], T_0 is the receiver optical throughput (or one way transmission), A is the surface area of the

[3]Our on-line and off-line wavelengths are separated by 3 nm. Using the manufacturer's nominal curves, we calculated a change in η from the on-line to the off-line wavelength of about 1 part in 1000, which is small compared to our other corrections and is equivalent to an error in the energy monitor ratio, which is explicitly corrected for. Similarly, any errors in T_0 will be implicitly corrected for with the energy monitor correction.

telescope, E_{on} and E_{off} are the on-line and off-line laser output energies, α_p and α_m the aerosol (particulate) and Rayleigh (molecular) extinction coefficients, β_p and β_m the aerosol and Rayleigh backscatter coefficients, K the oxygen resonant absorption coefficient which is essentially zero at the off-line frequency we selected for the pressure measurements, z is the altitude, z_{ref} is the aircraft altitude. The normal DIAL simplyfing assumption of ignoring any wavelength dependence of all variables except K is made for the moment to effect a solution for pressure. The wavelength dependence of the extinction and backscatter coefficients will be treated in the next section on atmospheric effects. Introducing equations (4a) and (4b) in equation (3), we find:

$$\tau(z) = \exp\left(-2\int_{z_{ref}}^{z} K(r)\,dr\right). \tag{5}$$

The measured transmission for each altitude is computed from the lidar return signals using equation (3), in the region between the gating turn-on transient and the surface return. Korb and Weng (1983) states that the one way oxygen absorption optical depth is:

$$\int_{z_{ref}}^{z} K(r)\,dr = C \mid p^2(z) - p^2(z_{ref}) \mid, \tag{6}$$

where $p(z)$ and $p(z_{ref})$ are the pressure at altitudes z and z_{ref} and C is an experimentally determined calibration constant. Higher order terms can be neglected for the limited range of altitudes encountered in our experimental measurements. Solving for $p(z)$,

$$p(z) = \left(-\frac{1}{2}\frac{\ln \tau(z_{ref}, z)}{C} + p^2(z_{ref})\right)^{1/2}. \tag{7}$$

$p(z_{ref})$ is acquired with the NEMS on the aircraft and z_{ref} is measured with the altimeter channel of the lidar system. $\tau(z_{ref}, z)$ is the lidar measured

atmospheric transmission with a correction applied for systematic errors in the measurement of the ratio of the laser energies. Next we describe the method used to find the calibration constant C and the laser energy ratio correction to the measured transmissions.

It was observed that the transmission calculated from equation (3) and extrapolated back to the altitude of the aircraft was not unity (Figure 1). We attribute this to an error in the measurement of the relative energy in each laser pulse based on a laboratory assessment using two similar photodiode detectors. A systematic correction was developed, as part of the absolute calibration, based on the lidar data and balloon sounding in order to force the transmission to one at the aircraft altitude. Let us consider two regions of the atmosphere sampled by the lidar: the near field and the far field. Let $\tau_m(z_{ref}, z)$ be the lidar measured transmission between the aircraft and altitude z. If both the transmission measured in the far field and in the near field are in error by the same factor then we can determine the correct transmission for the atmospheric path between the near and far fields by the ratio of the two measured transmissions:

$$\frac{\tau_m(z_{ref}, z_{far})}{\tau_m(z_{ref}, z_{near})} = \exp\left(-2\int_{z_{near}}^{z_{far}} K(r)\,dr\right). \tag{8}$$

Using equation (8) in equation (6) we solve for the calibration constant C:

$$C = -\frac{1}{2}\ln\frac{\tau_m(z_{ref}, z_{far})}{\tau_m(z_{ref}, z_{near})} / \mid p^2(z_{far}) - p^2(z_{near}) \mid . \tag{9}$$

Values of $p(z_{far})$ and $p(z_{near})$ are accurately estimated from the balloon sounding. Radar tracking of the target trailing the meteorological package provides us with the exact balloon altitude at all times. A parabola is fit to

these independent measurements of pressure (from radiosonde) and altitude (from radar) for the first 3000 m. The parabola is then used to interpolate between radiosonde data points to get the pressure at z_{far} and z_{near}. In order to minimize the calibration error due to noise in the measurements, values of the lidar measured transmissions are averaged over 180 m in altitude in the near and far fields. We calculate a value of C for the transmission profile taken nearest in time and space to a radiosonde profile.

To correct the measured transmission for the energy monitor error we first calculate the corrected transmission profile in the near field $\tau_c(z_{near})$, using equations (5), (6) and (9):

$$\tau_c(z_{ref}, z_{near}) = \exp\left(-2C \mid p^2(z_{near}) - p^2(z_{ref}) \mid\right). \tag{10}$$

The correction factor $\tau_c(z_{ref}, z_{near})/\tau_m(z_{ref}, z_{near})$ is then applied to the entire transmission profile. Finally, we have to account for the pitch and roll angles as they increase the path over which the absorption coefficient is calculated, while our relationship between optical depth and pressure is based on a vertical path. The corrected vertical transmission profile is given by:

$$\tau(z_{ref}, z) = \left(\tau_m(z_{ref}, z) \times \frac{\tau_c(z_{ref}, z_{near})}{\tau_m(z_{ref}, z_{near})}\right) \cos\theta_p \cos\theta_r. \tag{11}$$

Figure 2 shows an uncorrected and a corrected transmission profile made from measured lidar signals.

4. Atmospheric systematic effects on measured transmission

In this section we consider the effects of rotational Raman scattering, wavelength dependence of the aerosol backscatter coefficient, and Doppler broad-

ening in the presence of an isotopic oxygen line. All these processes require a knowledge of the relative contributions of Rayleigh and Mie scattering to the lidar signals. Therefore we first discuss the retrieval of the backscatter ratio R from the off-line signal, where we define R as:

$$R(z) = \frac{\beta_{p,off}(z) + \beta_{m,off}(z)}{\beta_{m,off}(z)}. \tag{12}$$

For the off-line channel, the received optical power at the PMT may be written as:

$$P_{off}(z) = \frac{A\,T_0}{(z_{ref} - z)^2}\,\eta\,E_{off}\,\frac{c}{2}\,\beta_{off}(z)\,\exp\left(-2\int_{z_{ref}}^{z}\alpha_{off}(r)\,dr\right), \tag{13}$$

where β_{off} and α_{off} represent the total (Rayleigh + Mie) backscatter and extinction coefficients. We solve equations (13) and (2) for the attenuated backscatter coefficient in terms of the off-line measured signal:

$$\beta_{off}(z)\,\exp\left(-2\int_{z_{ref}}^{z}\alpha_{off}(r)\,dr\right) = C^*\,(z_{ref} - z)^2\,S_{off}(z), \tag{14}$$

where C^* is the lumped constant, and $(z_{ref} - z)^2\,S_{off}(z)$ is the range-squared, energy normalized signal.

If we assume for the moment that the total (aerosol plus molecular) backscatter to extinction ratio, $\phi_{off}(z) = \beta_{off}(z)/\alpha_{off}(z)$ is constant with altitude, we may then write:

$$\beta_{off}(z)\,\exp\left(-\frac{2}{\phi_{off}(z)}\int_{z_{ref}}^{z}\beta_{off}(r)\,dr\right) = C^*\,(z_{ref} - z)^2\,S_{off}(z) \tag{15}$$

that may be integrated from z_{ref} to z :

$$\int_{z_{ref}}^{z}\beta_{off}(r')\,\exp\left(-\frac{2}{\phi_{off}(z)}\int_{z_{ref}}^{r'}\beta_{off}(r)\,dr\right)\,dr' \;=$$
$$\frac{\phi_{off}(z)}{2}\left(1 - \exp\left(-\frac{2}{\phi_{off}(z)}\int_{z_{ref}}^{z}\beta_{off}(r)\,dr\right)\right). \tag{16}$$

Combining equations (15) and (16) and integrated over altitude, we find :

$$\beta_{off}(z) = \frac{(z_{ref} - z)^2 \, S_{off}(z)}{\frac{1}{C^*} - \frac{2}{\phi_{off}(z)} \int_{z_{ref}}^{z} (z_{ref} - r)^2 \, S_{off}(r) \, dr}, \tag{17}$$

which is equivalent to the solution for the lidar equation found by Klett (1981). For surface wind speeds over the open ocean smaller than 3 $\mathrm{m\,s^{-1}}$, Trouillet *et al.* (1997) have found that the optical depth resulting from aerosol production at the sea surface was not sufficient for the extinction to be large enough to make the second term in the denominator significant when compared to the first term. Therefore we can approximate equation (17) as:

$$\beta_{off}(z) = C^* \, (z_{ref} - z)^2 \, S_{off}(z). \tag{18}$$

In order to determine a solution to the backscatter ratio, we apply a boundary condition to the level in the atmosphere that presents the smallest signal variance. By examining the range-squared corrected signals, this region was found near 2 km altitude and is discussed in further details in Part II. Trouillet *et al.* (1997) have shown that a reference value of the total backscatter coefficient near the surface could be derived from the lidar signal in the PBL and the intensity of the surface return (provided that it is not saturated), which in turn relates to sea-surface reflectance and surface wind speed (Cox and Munk, 1954; Bufton *et al.*, 1983). However, in the case of the pressure measurements detailed in Part II, the surface return was saturated and this method could not be used successfully.

Trouillet *et al.* (1997), during SOFIA and SEMAPHORE[4], as well as

[4]The SOFIA campaign took place over the Azores in June of 1992 as part of the Atlantic STratocumulus EXperiment. The SEMAPHORE campaigh took place in the same region in October of 1993.

Flamant and Pelon (1996), during PYREX[5], have reported values of the scattering ratio of R=1.5 at an altitude of 2 km above the Atlantic and the Mediterranean, respectively. These values were obtained from extinction measurements made around 0.5 μm by a nephelometer carried onboard an aircraft. At a wavelength of 760 nm, the value of this ratio is expected to be larger, although values of R=1.2 have been observed (Sasano and Browell, 1989). In order to estimate the errors on the pressure retrievals caused by rotational Raman scattering, the wavelength dependence of the aerosol backscatter coefficient, and Doppler broadening in the presence of an isotopic oxygen line, the boundary condition of R=1.5$\pm$0.3 at 2 km is taken in the following sections.

The ratio of the off-line lidar signal in the PBL to the off-line lidar signal in the free troposphere varies between 2 and 3, on average. The backscatter ratio in the PBL will then range from 2.4 to 5.4, if we assume the transmission to be small. On figure 3 we show representative backscatter ratio profile calculated from our data in nearly neutral stratification conditions with R equal to 1.2, 1.5 and 1.8. In slightly unstable condition, this ratio is expected to be larger.

a. Rotational Raman scattering

The measurements under consideration in Part II were taken at night with a broadband optical filter in the receiver which failed to exclude rotational Raman scattering from the lidar signals. We need to account for rotational Raman scattering by oxygen and nitrogen since most of this light will be

[5]The PYREX campaign was deployed in the Pyrénées region at the French-Spanish border in October and November of 1990.

unabsorbed by oxygen on its way back to the receiver. The total amount of Raman scattering from these two molecules is on the order of 3.5% of the Rayleigh scattering (Korb *et al.*, 1995). We may neglect vibration-rotation Raman scattering as it is another two orders of magnitude smaller than this. Use of a 1 nm bandpass filter would exclude rotational Raman scattering from the measured signals. This would require an off-line wavelength closer to the on-line wavelength.

To account for Raman scattering in the lidar detected optical power for the on-line signal, we separate the measured O_2 transmission into its particulate and molecular backscatter components including a term to account for the Raman backscatter as

$$\tau(z)_{meas} = \left[\frac{(\beta_p(z) + \beta_m(z))\,\tau_{O_2}(z) + 0.035\,\beta_m(z) T_{O_2}(z)}{\beta_p(z) + \beta_m(z) + 0.035\,\beta_m(z)}\right]. \qquad (19)$$

In equation (19), τ_{O_2} and T_{O_2} are the 2-way and 1-way O_2 transmission respectively, and $0.035 \times \beta_m$ is the Raman backscatter coefficient. The Raman component of the signal has only the one-way O_2 absorption imposed on the laser light on the outgoing path from the lidar. There is essentially no oxygen resonant extinction for the Raman backscattered signal because of the frequency shift, except for any coincidences between O_2 absorption and rotational Raman lines which we have calculated to be an insignificant fraction of the total Raman signal. The fraction of the on-line signal due to Raman scattering will decrease as the aerosol scattering component increases, so that this effect will be important in relatively aerosol-free atmospheres. We can evaluate the extent of this effect on the measured O_2 transmission by using the scattering ratio estimated from the off-line signals.

If $\partial\tau/\tau$ is the fractional difference in the measured transmission and the desired (non-Raman contaminated) transmission, it follows from equation (19) that:

$$\begin{aligned}\frac{\partial\tau(z)}{\tau(z)} &= \frac{\tau_{meas}(z) - \tau_{O_2}(z)}{\tau_{O_2}(z)} \\ &= \left[\frac{R(z) + 0.035\,/\,T_{O_2}(z)}{R(z) + 0.035}\right] - 1. \end{aligned} \tag{20}$$

Differentiating equation (7) with the 2-way transmission, we get:

$$\partial p(z) = -\frac{1}{4\,C\,p(z)}\frac{\partial\tau(z)}{\tau(z)}. \tag{21}$$

Combining equations (20) and (21) :

$$\partial p(z) = -\frac{1}{4\,C\,p(z)}\left(\left[\frac{R(z) + 0.035\,/\,T_{O_2}(z)}{R(z) + 0.035}\right] - 1\right). \tag{22}$$

Figure 4 shows the error in the retrieved pressure field from neglecting the effect of the rotational Raman scattering. This was calculated from equation (22) using the data from Figures 2 and 3. The error increases with range in the free troposphere, since the backscattered signal is more strongly absorbed and a larger fraction of the measured total signal is contributed by Raman scattering. The error temporarily drops as the beam penetrates the mixed layer due to the sudden increase in aerosol backscatter, then continues as the absorption increases. The Raman signal component causes a maximum error of about -10 hPa near the surface. The constant slope of this error will be, in large part, removed by the calibration procedure described in Section 3.d, leaving the residual error caused by aerosol gradients. From Figure 4, one can see that when the signal goes from relatively clear air into a region of high aerosol content, a jump in pressure will be observed in the retrieval (between 1600 m and 1300 m).

b. Elastic scattering spectral considerations

The two main scattering phenomena in the atmosphere are Mie scattering for aerosols and Rayleigh scattering for molecules. For Rayleigh scattering, the laser line shape will be broadened by the Brownian motion of the molecular scatterers. Aerosol scattering is not affected by Doppler broadening. The dial technique for pressure measurements uses the existence of an absorption trough, the region of minimum absorption between two closely spaced strongly absorbed oxygen lines. The trough is formed by the wings of the nearest collision broadened lines where the absorption is pressure sensitive. The lines are selected so that the resultant measurement will be temperature insensitive. The on- line frequency was taken in the trough region between 13150 cm^{-1} and 13154 cm^{-1}, and the off- line frequency in a nearby location with minimal resonant absorption but nearly identical attenuation due to scattering and continuum absorption. For the off-line detected optical power, we use a simplified form of the lidar equation that uses spectrally integrated quantities:

$$P_{off}(z) = \frac{T_0\, A\, \eta}{(z_{ref} - z)^2}\, E_{off}\, \frac{c}{2} \left(T^c_{off}(z)\right)^2 \left[\beta_{p,off}(z) + \beta_{m,off}(z)\right], \qquad (23a)$$

and for the on-line detected power, we write :

$$\begin{aligned} P_{on}(z) \;=\; & \frac{T_0\, A\, \eta}{(z_{ref} - z)^2}\, E_{on}\, \frac{c}{2} \left(T^c_{on}(z)\right)^2 \\ & \left[\beta_{p,on}(z)\, T^p_{on}(z)\, T^L_{on}(z) + \beta_{m,on}(z)\, T^m_{on}(z)\, T^L_{on}(z)\right], \end{aligned} \qquad (23b)$$

where $T^c_\nu(z)$ is the one way transmission due to scattering and continuum absorption effects, $T^L_\nu(z)$ is the one way transmission of the laser initial line

shape due to resonant absorption effects and $T_\nu^p(z)$ is the resonant one way transmission on the return path for the Mie scattering. $T_\nu^p(z)$ and $T_\nu^L(z)$ are nearly identical since the signal is elastically scattered by aerosols, with no change in the shape of the initial spectrum other than the modification it undergoes as a result of the spectral structure of the absorption trough. $T_\nu^m(z)$ is the resonant one way transmission experienced by the Doppler broadened Rayleigh backscatter on the return path. Even though the O_2 trough is significantly broader (1.5 cm^{-1}) than the initial laser line (0.015 cm^{-1} at FWHM) and the double Doppler broadened backscattered line shape ($\approx$0.06 cm^{-1} at FWHM), the fact that it is not flat will affect the measurements: the larger the line width, the larger the $\int K(\nu)dr$ associated with the line shape on the return path. Using equations (23a) and (23b) in equation (3), and implementing the usual DIAL assumption that the continuum backscatter coefficient and transmission are equal at the two closely spaced on-line and off-line wavelengths, the overall optical depth between the reference altitude and altitude z can be expressed as:

$$\int_{z_{ref}}^{z} K(\nu,r)\,dr = \frac{\beta_p(z)}{\beta_p(z)+\beta_m(z)} \int_{z_{ref}}^{z} K_p(\nu,r)\,dr + \frac{\beta_m(z)}{\beta_p(z)+\beta_m(z)} \int_{z_{ref}}^{z} K_m(\nu,r)\,dr, \qquad (24)$$

where $\int K_p(\nu,r)\,dr$ is the optical depth associated with Mie particle scattering and $\int K_m(\nu,r)\,dr$ is the optical depth associated with Rayleigh molecular scattering. Aerosols will increase the aerosol to total backscatter ratio (the first term on the right-hand side of the equation), therefore reducing the overall value of $\int K(\nu,r)\,dr$ because $\int K_p(\nu,r)\,dr$ is smaller than $\int K_m(\nu,r)\,dr$. Note that this is the opposite effect observed in H_2O DIAL measurements

(Ansmann, 1985) and O_2 temperature DIAL measurements (Theopold and Bosenberg, 1993) since we operate at an absorption local minimum rather than a local maximum. This effect is minor however when compared to the effects described in the next two sections.

c. Aerosol extinction and backscatter coefficients wavelength dependence

The transmission expressed in equation (5) assumes the attenuation due to scattering and continuum absorption to be nearly identical for the on-line and off-line wavelengths. We now drop that assumption to investigate the impact of the wavelength dependence of the extinction and backscatter coefficients (between the on-line and the off-line wavelengths) on the pressure measurements. We still consider these coefficients to have minimal change over the small spectral intervals covered by the backscatter line shapes, however. From equations (23a) and (23b), equation (3) can be rewritten as:

$$\begin{aligned} \tau(z)_{meas} &= \left(\frac{T^c_{on}(z)}{T^c_{off}(z)}\right)^2 \frac{\beta_{p,on}(z)T^p_{on}(z)T^L_{on}(z) + \beta_{m,on}(z)T^m_{on}(z)T^L_{on}(z)}{\beta_{p,off}(z) + \beta_{m,off}(z)} \\ &= \left(\frac{T^c_{on}(z)}{T^c_{off}(z)}\right)^2 \frac{\beta_{p,on}(z) + \beta_{m,on}(z)}{\beta_{p,off}(z) + \beta_{m,off}(z)}\tau(z) \end{aligned} \tag{25}$$

The first part of the right hand side can be considered as a correction to transmission as calculated assuming the aerosol extinction and backscatter coefficients to be insensitive to wavelength (i.e. the $\tau(z)$ of equation (5)).

If $\partial\tau/\tau$ is the fractional difference in the measured transmission and the desired transmission, equation (25) can be used:

$$\begin{aligned} \frac{\partial\tau(z)}{\tau(z)} &= \frac{\tau(z)_{meas} - \tau(z)}{\tau(z)} \\ &= \left(\frac{T^c_{on}(z)}{T^c_{off}(z)}\right)^2 \frac{\beta_{p,on}(z) + \beta_{m,on}(z)}{\beta_{p,off}(z) + \beta_{m,off}(z)} - 1 \end{aligned}$$

(26)

In order to get the error induced in the pressure retrieval, we combine equations (21) and (26):

$$\partial p(z) = -\frac{1}{4\,C\,p(z)} \left(\left(\frac{T^c_{on}(z)}{T^c_{off}(z)} \right)^2 \frac{\beta_{p,on}(z) + \beta_{m,on}(z)}{\beta_{p,off}(z) + \beta_{m,off}(z)} - 1 \right). \qquad (27)$$

The impact of the aerosol wavelength dependence for DIAL measurements made over the Atlantic (Part II) was tested using the maritime aerosol model described by Trouillet *et al.* (1997). Based on the works of Voltz (1973), Shettle and Fenn (1979) and d'Almeida *et al.* (1991), the model assumes a lognormal size distribution for the combination of sulfate and sea-salt aerosols in the lower troposphere. Since lidar signal intensity is very sensitive to relative humidity (Dupont *et al.*, 1994), the aerosol refractive index dependence on relative humidity is also introduced and modeled according to relationships previously proposed by Hänel (1971; 1972) and d'Almeida *et al.* (1991). The relative fractional occupation rate of the two modal radii depends on the surface wind speed. This rate is assumed constant in the PBL for a given wind speed. Aloft, in order to account for the decreasing sea-salt aerosol concentration, a 2 km height scale (Blanchard and Woodcock, 1980) is introduced.

A Mie model is used to calculate the backscatter and extinction coefficients for the sulfate and sea-salt aerosols at 757 nm (corresponding to the off-line wavelength of the DIAL system). The maritime particulate mixture phase function profile is then deduced from a relative humidity profile and the fractional concentration of sea-salt dependence with height. The sulfate and sea-salt aerosol backscatter and extinction coefficients wavelength de-

pendence are calculated according to:

$$\delta_\alpha = \frac{\ln(\alpha(\lambda_2)/\alpha(\lambda_1))}{\ln(\lambda_2/\lambda_1)} \qquad \text{for} \qquad \lambda_2 \geq \lambda_1 \tag{28a}$$

and

$$\delta_\beta = \frac{\ln(\beta(\lambda_2)/\beta(\lambda_1))}{\ln(\lambda_2/\lambda_1)} \qquad \text{for} \qquad \lambda_2 \geq \lambda_1 \tag{28b}$$

where $\lambda_2 = 757$ nm and $\lambda_1 = 532$ nm. The Ängstrom coefficients δ_α and δ_β calculated from equations (28a) and (28b) will be used to estimate the difference in transmission between the on-line and off-line wavelength given by equation (26). However, δ_α and δ_β also depend on relative humidity. Since we expect typical values to be quite different in the free troposphere and in the boundary layer, the humidity profile measured at Wallops was used to calculate these coefficients throughtout the lower troposphere. Table 1 summarizes the value of the Ängstrom coefficients for extinction and backscatter for relative humidities of 10% and 50%, representative of the free troposphere and the boundary layer, respectively.

Because wind measurements were taken only at Wallops and not above the ocean, we show the resulting error for a surface wind speed ranging from 3 to 7 $\mathrm{m\,s^{-1}}$ (Figure 5). The error induced by this uncertainty is negligible, in comparison to the error resulting from the vertical aerosol distribution. The latter effect induces an error that is largest in the free troposphere. This is caused by (i) the large wavelength dependence of molecular extinction and backscatter coefficients ($\delta \approx -4$) and (ii) the fact that sulfate aerosols dominate the particulate scattering in a region where their scattering properties strongly depend on wavelength (for low values of the relative humidity, see Table 1). In the PBL, sea-salt aerosols control the particle scattering but

their hydroscopic properties prevents any strong wavelength dependence of the extinction and backscatter coefficients. This will result in a pressure discontinuity at the top of the PBL because of the strong aerosol gradient. Note that the error does not depend on the value of scattering ratio chosen as a boundary condition (equation (27)).

d. Isotopic oxygen lines

Isotopic lines have been observed in the O_2 spectrum in long-path atmospheric spectroscopic measurements by Babcock and Herzberg (1948). From their measurements one expects to observe an $O^{16} - O^{18}$ line in the center of the trough we used for pressure measurements. Figure 6 shows a calculated absorption spectrum near the 1000 hPa level assuming a line strength equal to the strength of the same transition in $O^{16} - O^{16}$. We attempted to locate this line with the lidar in flight by tuning the laser across the absorption trough while observing a real-time display of atmospheric transmission integrated over a portion of the path below the aircraft. We failed to observe the isotopic line due to inadequate signal to noise over reasonable integration times of a few seconds. Alternatively, we located the laser frequency where we thought it should be to avoid the isotopic line by interpolating between the sides of the $O^{16} - O^{16}$ lines as measured on the real-time display. However, this technique may also be of questionable accuracy for the same reason we failed to observe the isotopic line. Therefore, we studied what would happen if the laser were actually located on the isotopic line.

To help visualize the spectral processes, refer to figure 6, where we have plotted the O_2 spectrum in the boundary layer with and without the isotopic

line, the laser output spectrum, and the Rayleigh broadened component of the laser backscatter. The isotopic line adds about 30% to the trough absorption at the line center. Note that the collision broadened line profile central absorption is altitude independent since the decrease in absorption due to a redistribution of the molecular population into the wings of the profile due to increasing pressure is exactly offset by the increase in density (Korb and Weng, 1982). Therefore this additional absorption, to first order, is pressure independent in the center, gradually changing over to a p^2 dependence as the frequency moves further from line center. The laser spectrum was measured by Korb *et al.* (1995) to consist of three nearly equally spaced modes separated by 0.007 cm^{-1}, the two outer modes being half as intense as the central mode. The laser spectrum envelope can be approximated by a Gaussian profile with a half width equal to the mode spacing.

For a description of the mathematical representation of the lidar formulation which includes the frequency dependence of the laser light and Rayleigh scattering, we refer the reader to Ansmann and Bosenberg (1987).

For the purposes of modeling the effect of the isotopic line absorption on the Rayleigh broadened and aerosol backscatter, we use three modeled atmospheres having backscatter profiles similar to our data, represented in Figure 7. We calculated lidar signals using our system parameters, with the on-line signals as a function of frequency. Figure 8 represents the on-line return signal spectra at 4 altitude levels in an atmosphere characterized by a backscatter ratio of 5 in the PBL and 1.2 in the free troposphere. The outgoing laser energy is concentrated within the isotopic absorption line, hence experiences a stronger absorption coefficient. The backscattered energy

is distributed into the wings of the isotopic line and experiences a smaller spectrally integrated absorption coefficient. With the laser centered on the isotopic line, the immediate effect of the aerosols is to force more of the backscatter into the isotopic absorption line, therefore increasing the net absorption. As the laser beam propagates down through the atmosphere, its spectral shape changes, broadening if centered on the isotopic line, or if off-center, becoming asymmetric. This effect is minor compared to the variation in aerosol scattering, however. The net 30% offset in the absorption baseline due to the presence of the isotopic line is not a source of error since it acts as a net change to the $O^{16} - O^{16}$ line strength, which is accounted for in the calibration procedure discussed in the section on instrumental errors.

To evaluate the error in the retrieved pressure profiles caused by ignoring the effect of Rayleigh broadening in the presence of the isotopic line, we analyze the oxygen transmission calculated for combined aerosol and molecular scattering and compare it to the oxygen transmission calculated for molecular scattering only. We could compare it to aerosol only scattering which would more closely conform to the lidar assumption of monochromicity, but chose pure Rayleigh scattering for consistency with our other corrections and the more realistic limit of having zero aerosols as opposed to zero molecules. We define a correction factor, τ^*, to be applied to the measured transmission, that will yield the transmission we should get in the absence of aerosols, τ_m:

$$\tau^* = \frac{\tau_{meas}}{\tau_m} \tag{29}$$

where τ_{meas} can be found from the optical depth (equation 24):

$$\tau_{meas}(z) = \exp\left(-2\frac{\beta_p(z)}{\beta_p(z)+\beta_m(z)}\int_{z_{ref}}^{z} K_p(r)\,dr\right)$$

$$\times \exp\left(-2\frac{\beta_m(z)}{\beta_p(z)+\beta_m(z)}\int_{z_{ref}}^{z} K_m(r)\,dr\right), \qquad (30)$$

and

$$\tau_m = \exp\left(-2\int_{z_{ref}}^{z} K_m(r)\,dr\right), \qquad (31)$$

where we have integrated the absorption coefficients K_p and K_m over the spectrum. Taking the ratio of τ_{meas} to τ_m and expressing the backscatter coefficient in terms of scattering ratio $R(z)$:

$$\begin{aligned}\tau^*(z) &= \exp\left[-2\left(1-\frac{1}{R(z)}\right)\left(\int_{z_{ref}}^{z} K_p(r)\,dr - \int_{z_{ref}}^{z} K_m(r)\,dr\right)\right] \\ &= \left(\frac{\tau_p}{\tau_m}\right)^{(1-1/R(z))}. \qquad (32)\end{aligned}$$

The oxygen transmission for the molecular scattered light and particulate scattered light are calculated using laboratory line parameters measured by Burch and Gryvnak (1969), and line frequencies measured by Babcock and Herzberg (1948), in a voigt line shape algorithm. Using equations 21, 26, and 32, we find the error induced in the pressure retrieval:

$$\partial p(z) = -\frac{1}{4\,C\,p(z)}\left(\tau^*(z)-1\right). \qquad (33)$$

Using the modeled lidar backscatter profiles from Figure 7, we estimate the errors in the pressure profile caused by not accounting for isotopic absorption using equations (32) and (33), plotting the results in Figure 9. Because aerosol scattering is concentrated at the line center, the effective absorption coefficient is larger for aerosol backscatter than for molecular backscatter. Hence, the model with greater aerosol scattering in the free troposphere shows larger pressure errors. The increased aerosol backscatter from the PBL causes even higher errors. From this figure, one can see that any aerosol structure

will create a correlated false structure in the retreived pressure field. But what happens when the laser frequency is somewhere else in relation to the isotopic line? This is illustrated in Figure 10, where we have plotted the errors for the worst case model, and having the laser located at one, two, and three half-widths from the isotopic line center, as well as on line center. At one half-width, the laser is centered on a linear region on the side of the line profile. Refer back to Figure 6 to help visualize this. If one spectrally integrates over the molecular backscatter lineshape, the effective absorption coefficient is about the same as that for the aerosol line shape, since energy on the higher absorbing side of the laser center frequency is compensated for by lower absorption on the opposite side. This is why the errors are close to zero at all altitudes. When the laser is located at two half-widths from the isotopic line center, the molecular backscatter contains a larger portion of energy in the isotopic line than does the aerosol backscatter. Hence the spectrally integrated absorption coefficient is larger for molecular than for aerosol backscatter, and the errors are negative instead of positive. As the laser is located even further from line center, the errors will decrease in magnitude, as does the curve for three half-widths away in Figure 10.

5. Summary and conclusion

We have analyzed the sensitivity of differential absorption lidar measurements of the atmospheric pressure profiles to instrumental and atmospheric systematic error sources. The errors are evaluated for airborne lidar measurements made off the mid-atlantic coast of the United States in 1989, as if they

were uncorrected for. They are summarized in Table 2. Large errors can result by ignoring the effects of Raman scattering, the wavelength dependence of extinction and backscatter coefficients, and interference by isotopic oxygen lines in the oxygen spectrum. All of these errors are strongly correlated with structure in the aerosol backscatter profiles and systematically add. They can introduce large pressure gradients on the horizontal since the lidar signal is highly sensitive to aerosol content and relative humidity which in turn relate, at small scales, to convective activity in the PBL, and, at larger scales, to stratification and coastal influence in terms of aerosol population. Accounting for their effects is also important on the vertical since pressure errors can be large in the free troposphere, a region where DIAL measurements are generally calibrated with respect to balloon data (see section 3.d).

A correction scheme is derived for each effect. These will be applied to pressure profile retrievals from the 1989 flight experiments in a companion paper, Part II, and the accuracy to which the retrievals are made will be evaluated.

Acknowledgements. Support for this work was provided by Dr. John Theon and Dr. Ramesh Kakar of NASA Headquarters; direction of Cyrille Flamant's grant by Pr. Thomas D. Wilkerson, technical support by Dr. Coorg Prasad, presently with Science and Engineering Services, Inc., Burtonsville, MD, and Mr. Joseph Famiglietti, NASA GSFC. The authors would also like to thank Dr. Patrick Chazette of CEA and Drs. Jacques Pelon, Pierre H. Flamant and Vincent Trouillet of CNRS for many helpful discussions.

References

[1] d'Almeida, G. A., P. Koepke, and E. P. Shettle, 1991: *Atmospheric aerosols, global climatology and radiative characteristics.* Adarsh Deepak Publishing, 124 pp.

[2] Anderson D., A. Hollingsworth, S. Uppala, and P. Woiceshyn, 1987: A study of the feasability of using sea and wind information from ERS-1 satellite. Part I: Wind scatterometer data. European Center for Medium Range Weather Forcasts contract report 6297/86/HGE-I(SC), 121 pp.

[3] Ansmann, A., 1985: Errors in ground-based water-vapor DIAL measurements due to Doppler- broadened Rayleigh backscatter. *Appl. Opt.,* **24,** 3476 3480.

[4] Ansmann, A., and J. Bosenberg, 1987: Correction scheme for spectral broadening by Rayleigh scattering in differential absorption lidar measurements of water vapor in the troposphere. *Appl. Opt.,* **26,** 3026 3032.

[5] Babcock, H. D., and L. Herzberg, 1948: Fine structure of the red system of atmospheric oxygen bands. *Astrophys. J.,* **108,** 167 190.

[6] Blanchard, C. D., and A. H. Woodcock, 1980: The production, concentration, and vertical distribution of the sea-salt aerosol. *Annals N. Y. Academy of Sciences,* 330 347.

[7] Bond, N. A., and R. G. Feagle, 1985: Structure of a cold front over the ocean. *Quart. J. Roy. Meteor. Soc.*, **111**, 739 759.

[8] Brown R. A., and G. Levy, 1986: Ocean surface pressure fields from satellite-sensed winds. *Mon. Wea. Rev.*, **114**, 2197 2206.

[9] Burch, D. E., and D. A. Gryvnak, 1969: Strengths, widths, and shapes of the oxygen lines near 13,100 cm^{-1} (7620 A). *Appl. Opt.*, **8**, 1493 1499.

[10] Bufton, J. L., F. E. Hodge, and R. N. Swift, 1983: Airborne measurements of laser backscatter from the ocean surface. *Appl. Opt.*, **22**, 2603 2618.

[11] Cox, C., and W. Munk, 1983: Measurements of roughness of the sea surface from photographs of the sun's glitter. *J. Opt. Soc. Am.*, **44**, 838 850.

[12] Dupont, E., J. Pelon, and C. Flamant, 1994: Study of the moist convective boundary layer structure by backscatter lidar. *Bound.-Layer Meteor.*, **69**, 1 25.

[13] Flamant, C., and J. Pelon, 1996: Atmospheric boundary-layer structure over the Mediterranean during a Tramontane event. *Quart. J. Roy. Meteor. Soc.*, **122**, 1741 1778.

[14] Flamant, C. N., G. K. Schwemmer, C.L. Korb, S. P. Palm, and K. D. Evans: Pressure measurements using an airborne differential absorption

lidar. Part II: Results from the 1989 Pressure Field Experiment. To be submitted to *J. Atmos. Ocean. Tech.*

[15] Hänel, G., 1971: New results concerning of visibility on relative Humidity and their Significance in Model for Visibility Forecast. *Beïtrage zur des Atmosphäre,* **44,** 137 167.

[16] Hänel, G., 1972: Computation of extinction of visible radiation by atmospheric aerosol particles as a function of the relative humidity based upon measured properties. *Aerosol science,* **3,** 377 386.

[17] Klett, J. D., 1981: Stable analytical inversion solution for processing lidar return. *Appl. Opt.,* **20,** 211 220.

[18] Korb, C. L., and C. Y. Weng, 1982: A theoretical study of a two wavelength lidar technique for the measurement of atmospheric temperature profiles. *J. Appl. Meteor.,* **21,** 1346 1355.

[19] Korb, C. L., and C. Y. Weng, 1983: Differential absorption lidar technique for measurement of the atmospheric pressure profile. *Appl. Opt.,* **22,** 3759 3770.

[20] Korb, C. L., G. K. Schwemmer, M. Dombrowski, and C. Y. Weng, 1989: Airborne and ground based lidar measurements of the atmospheric pressure profile. *Appl. Opt.,* **28,** 3015 3020.

[21] Korb, C. L., G. K. Schwemmer, J. Famiglietti, H. Walden, and C. Prasad, 1995: Differential absorption lidars for remote sensing of the

atmospheric pressure and temperature profiles: Final report. NASA Tech. Memo. 104618, 249 pp.

[22] Lee, H. S., G. K. Schwemmer, C. L. Korb, M. Dombrowski, and C. Prasad, 1989: Gated photomultiplier response characterization for DIAL measurements. *Appl. Opt.*,**29**, 3303 3315.

[23] Levy, G., and R. A. Brown, 1991: Southern hemisphere synoptic weather from a satellite scatterometer. *Mon. Wea. Rev.*, **119**, 2803 2813.

[24] Nuss, W., and R. A. Brown, 1987: Evaluation of surface winds and flux analysis in mid-latitude marine cyclones. *J. Dynamics of Atmospheres/Oceans*, **10**, 291 315.

[25] Sasano, Y., and E. V. Browell, 1989: Light scattering characteristics of various aerosol types derived from multiple wavelength lidar observations. *Appl. Opt.*, **28**, 1670 1679.

[26] Schwemmer, G. K., M. Dombrowski, C. L. Korb, J. Milrod, H. Walden, and R. H. Kagann, 1987: A lidar system for measuring atmospheric pressure and temperature profiles. *Rev. Sci. Instr.*, **58**, 2226 2237.

[27] Shettle, E. P., and R. W. Fenn, 1979: Models for aerosols of the lower atmosphere and the effects of humidity variations on their optical properties. Air Force Geophysics Laboratory Environment Research Papers, No 678, 94 pp. [AFGL-TR-79-0214.]

[28] Starr, D. O'C., C. L. Korb, G. K. Schwemmer, and C. Y. Weng, 1992: Observations of height- dependent pressure perturbation structure of a strong mesoscale gravity wave. *Mon. Wea. Rev.*, **120,** 2808 2820.

[29] Theopold, F., and J. Bosenberg, 1993: Differential absorption lidar measurements of atmospheric temperature profiles: Theory and experiment. *J. Atmos. Ocea. Tech.*, **10,** 165 179.

[30] Trouillet, V., J. Pelon, P. Chazette, and C. Flamant, 1997: Wind speed dependence of the atmospheric boundary layer optical properties and ocean surface reflectance as observed by airborne backscatter lidar. Submitted to *J. Atmos. Ocea. Tech.*

[31] Volz, F. E., 1973: Infrared optical constants of ammonium sulfate, sahara dust, volcanic pumice, and flyash. *Appl. Opt.*, **12,** 564 568.

Table 1: Wavelength dependence of the sea-salt and sulfate aerosols extinction and backscatter coefficients between 532 nm and 757 nm.

	Ängstrom coefficient			
Relative humidity	Extinction (δ_α)		Backscatter (δ_β)	
(%)	Sea-salt	Sulfate	Sea-salt	Sulfate
10	0.24	-1.34	-0.24	-1.38
50	1.03	0.13	0.82	0.26

Table 2: Systematic error on pressure retrievals caused by instrumental and atmospheric effects (in hPa).

	Atmospheric effects			Instrumental effects
	Rotational Raman	Wavelength dependence	Isotopic lines	Baseline subtraction
Free troposphere				
R = 1.2	-7 to -4	1.0 to 3	-0.3 to 0.7	0. to ±0.15
R = 1.8	-4 to -2	1.0 to 3	-0.8 to 2	0. to ±0.15
Boundary layer				
R = 2	-12 to -6	0. to 1	-1.2 to 3	0. to ±0.3
R = 5	-6 to -3	0. to 1	-2 to 5	0. to ±0.3

List of Figures

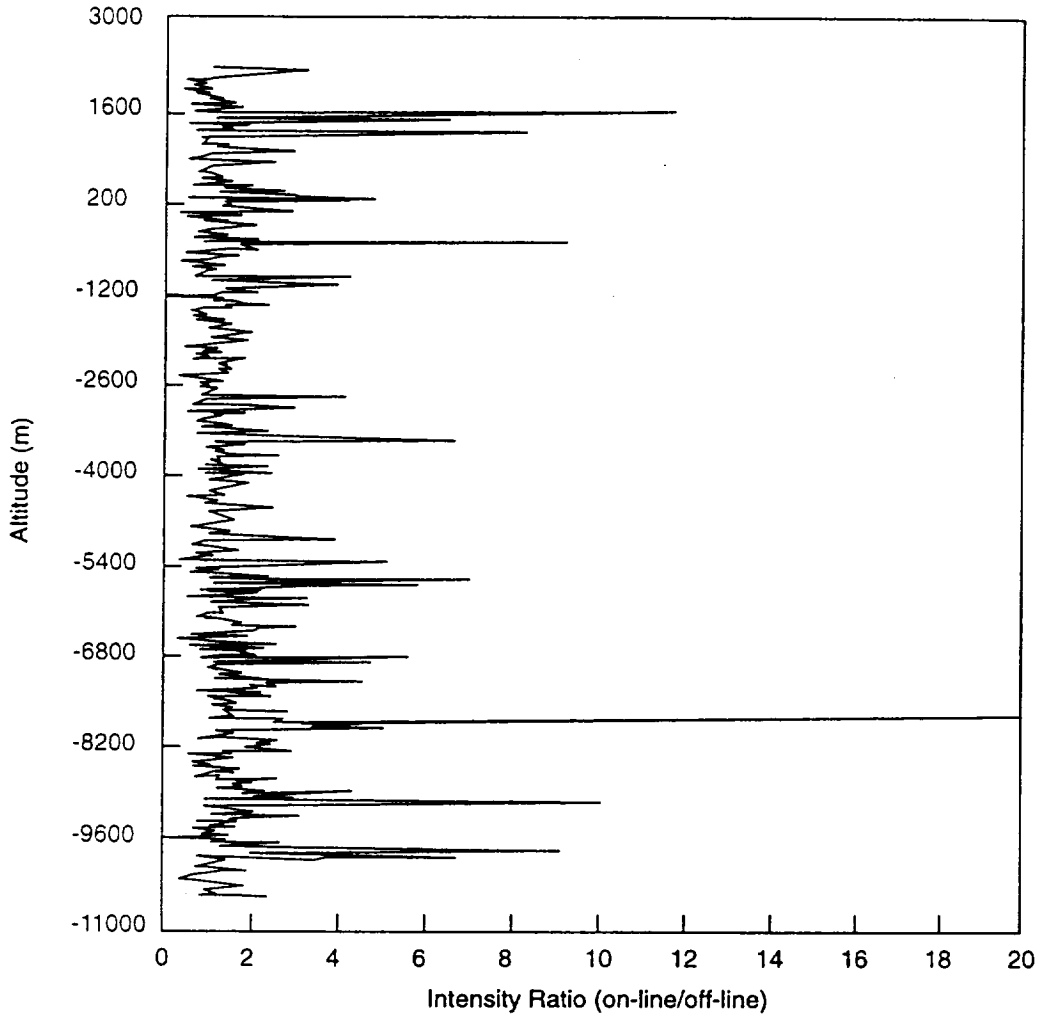

Figure 1: Ratio of the on-line to the off-line signal in the case where the laser beam is prevented from going out to the atmosphere. In the event that no ground loop affects the data, the signal detected for both acquisitions should be proportional to the atmospheric background, and the ratio of the on-line to the off-line should be equal to unity and constant with range. Noise in the data results from the small quantities being ratioed.

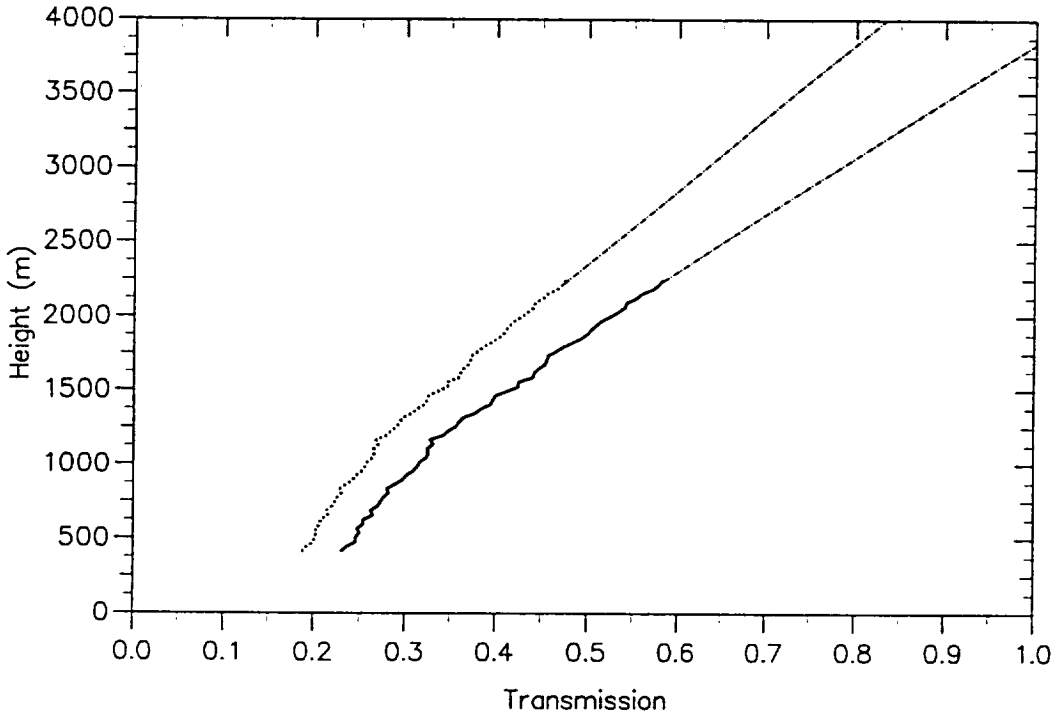

Figure 2: Oxygen transmission profile before (dashed line) and after (solid line) calibration using a pressure sounding. Note that only the corrected transmission profile goes through unity at the height of the aircraft (3800 m in this case).

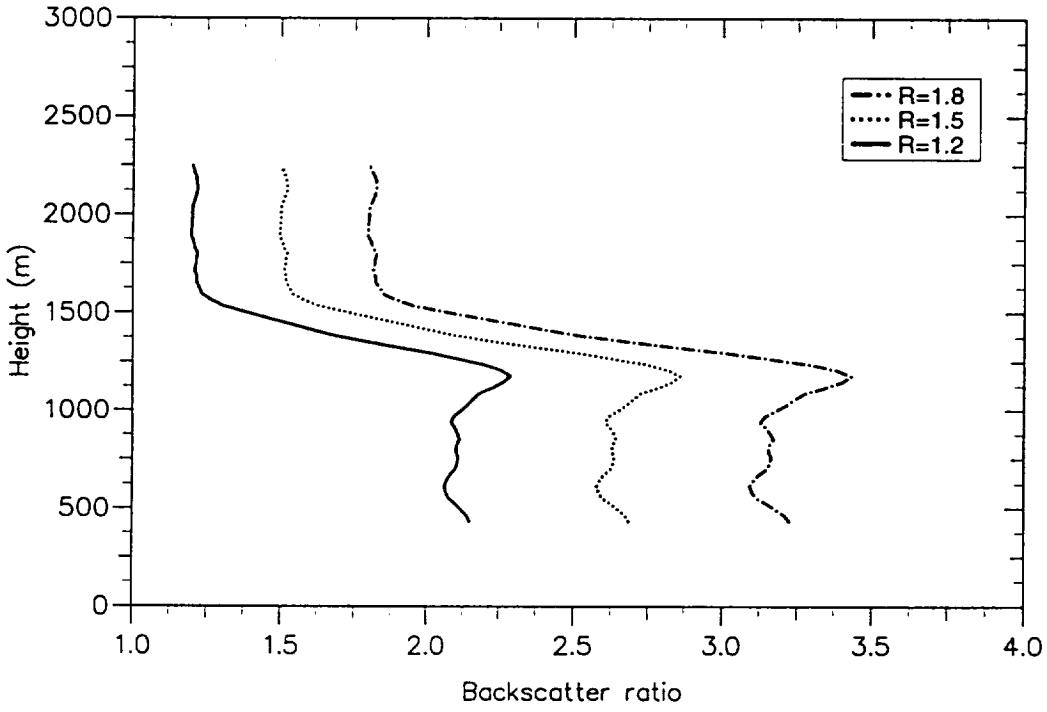

Figure 3: Scattering ratio profile derived from lidar measurements, made at 760 nm, during the 1989 Pressure Experiment. Profiles are given for three values of the scattering ratio boundary condition applied to the lidar signal profile at 2000 m.

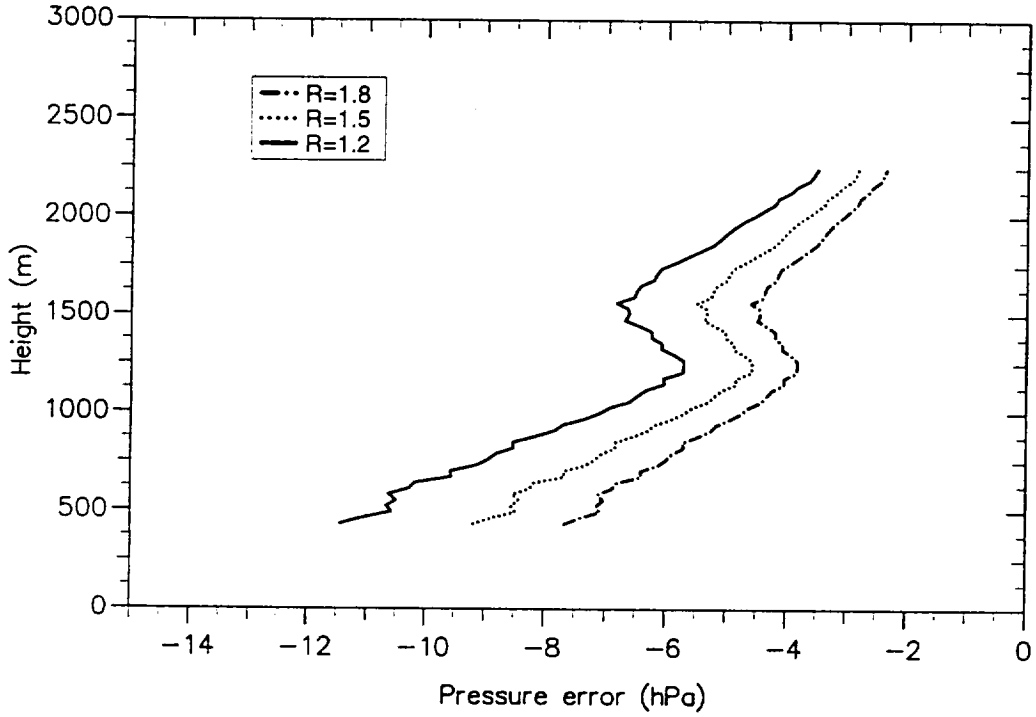

Figure 4: Pressure error when neglecting the effect of rotational Raman scattering.

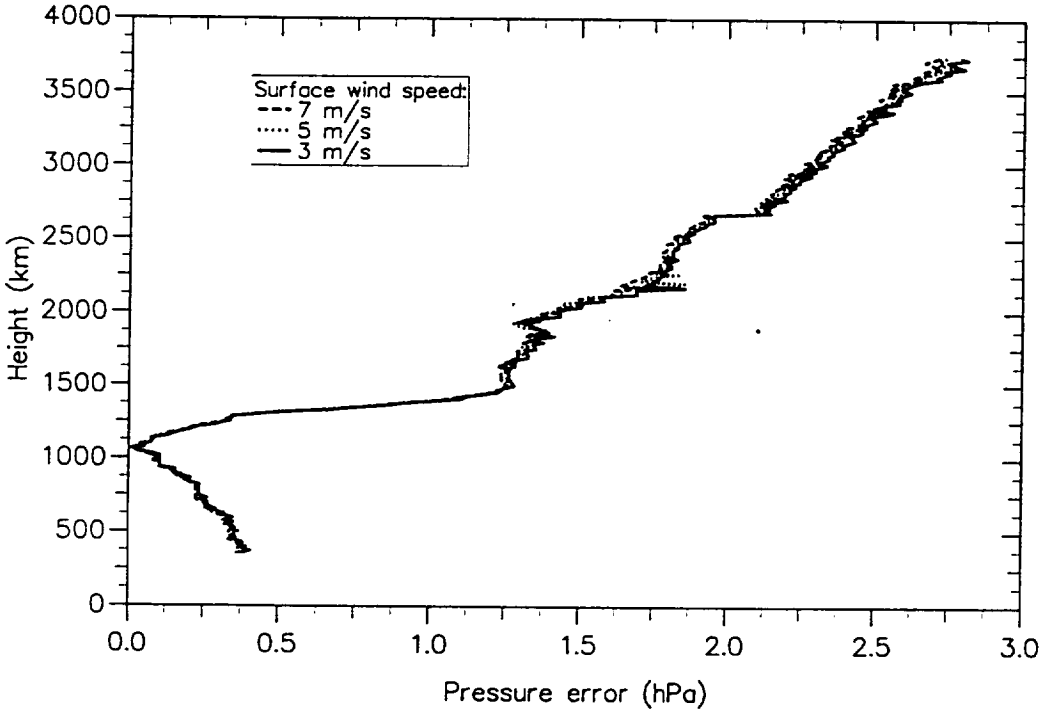

Figure 5: Pressure error when neglecting the effect of aerosol backscatter and extinction coefficients wavelength dependence.

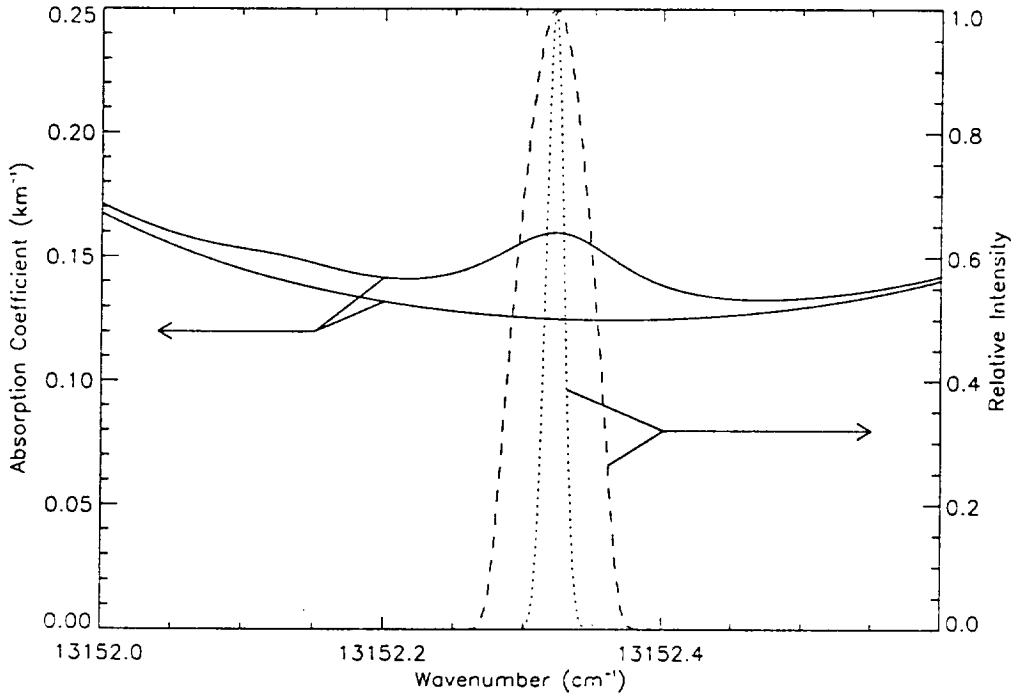

Figure 6: Calculated transmission spectrum (solid line) for O_2 in the region of the DIAL measurements, with and without the isotopic lines. Superimposed is the laser output spectrum (dotted line) and Rayleigh broadened backscatter (dashed line) relative to the O_2 absorption spectrum.

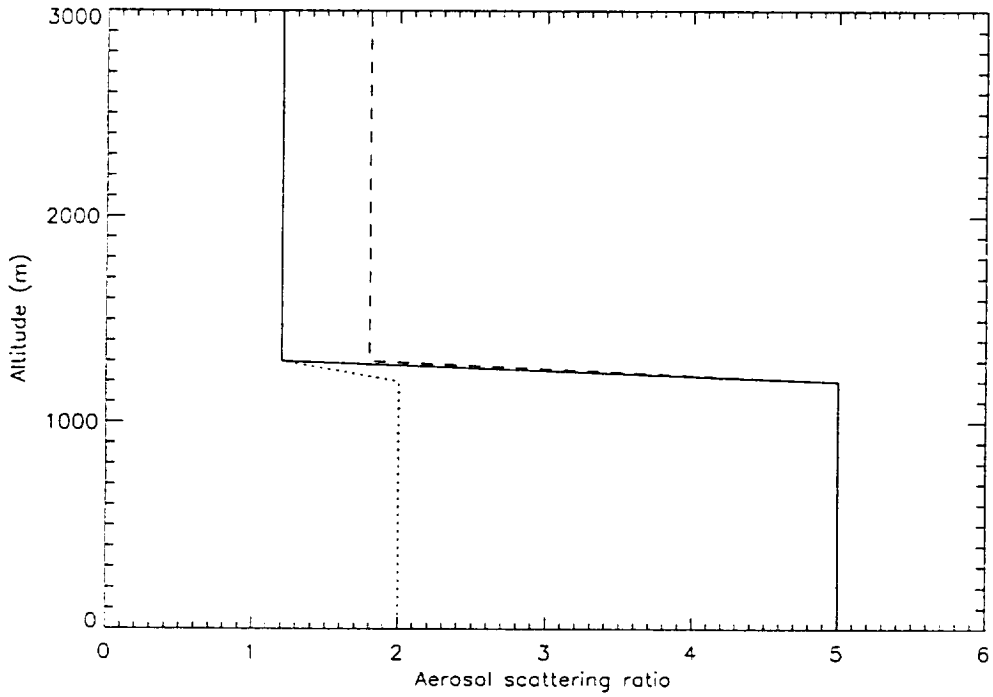

Figure 7: Backscatter ratio models used to calculate the effect of Rayleigh broadening in isotopic line effects. Two models use R=1.2 in the free troposphere with R=5 (solid line) and R=2 (dashed line) in the PBL. The third model (dotted line) uses R=1.8 in the free troposhere and R=5 in the PBL.

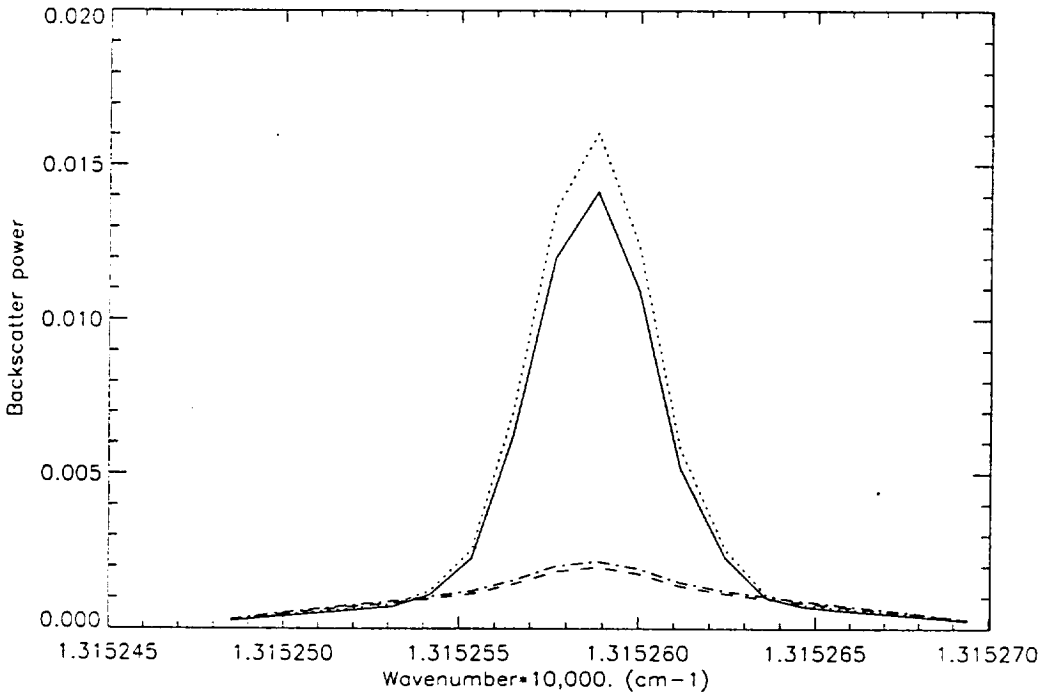

Figure 8: The on-line return signal spectra at various altitude levels, 100 m (solid line), 800 m (short-dashed line), 1500 m (long-dashed line) and 2200 m (short-and-long-dashed line), in an atmosphere characterized by a backscatter ratio of 5 in the boundary-layer.

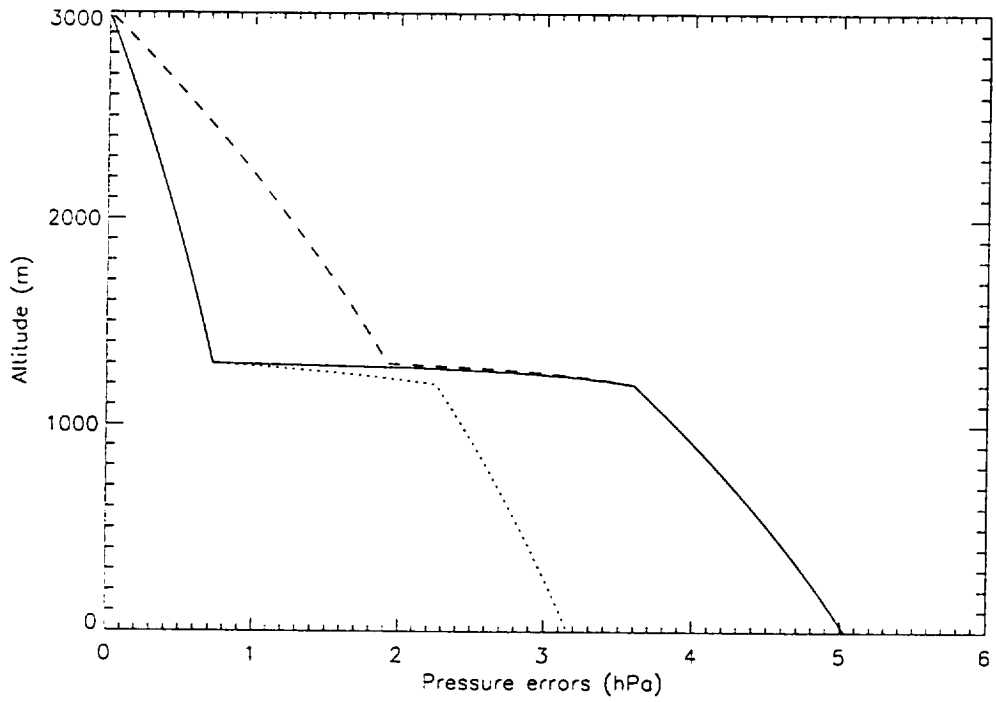

Figure 9: Errors in the retrieved pressure profile due to isotopic line interference. The line styles correspond to those representing their respective scattering models in Figure 7.

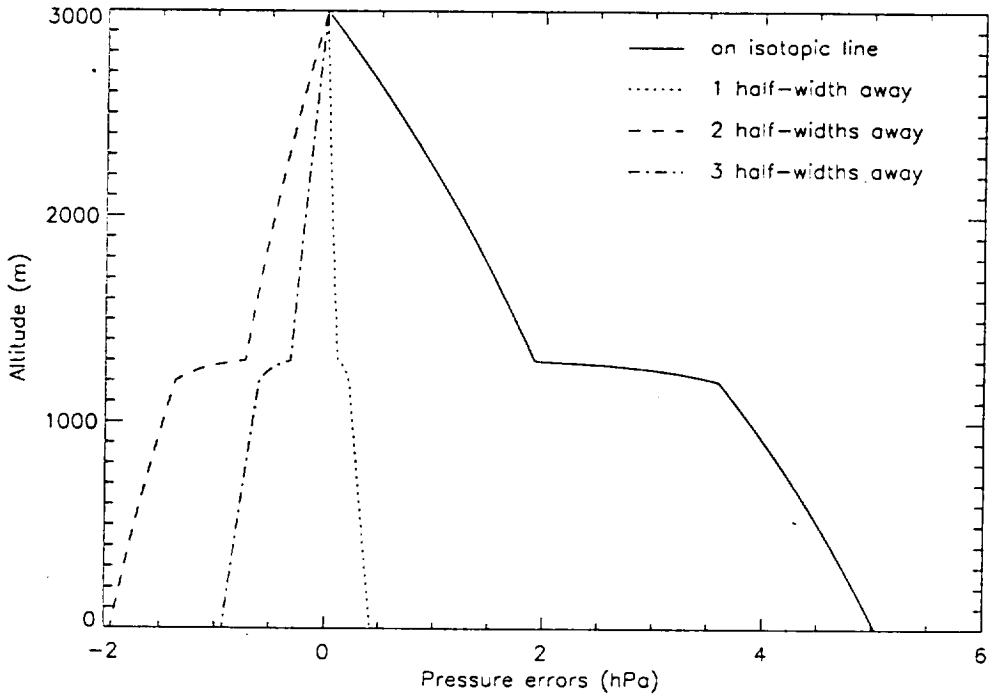

Figure 10: Pressure errors for the worst case aerosol model (R=1.8 in free troposphere and R=5 in PBL) due to the laser being on the isotopic line and the errors for the laser being one, two and three half-widths off the isotopic line.